



1 **Various lithospheric deformation patterns derived from**
2 **rheological contrasts between continental terranes:**
3 **Insights from 2-D numerical simulations**

4 Renxian Xie^{1,2}, Lin Chen³, Jason P. Morgan², Yongshun John Chen^{2*}

5 ¹School of Transportation Engineering, East China Jiaotong University, Nanchang, 330013, China

6 ²Department of Ocean Science and Engineering, Southern University of Science and Technology,
7 Shenzhen, 518055, China

8 ³State Key Laboratory of Lithospheric Evolution, Institute of Geology and Geophysics, Chinese
9 Academy of Sciences, Beijing, 100029, China

10 *Correspondence to:* Yongshun John Chen (johnyc@sustech.edu.cn)

11 **Abstract.** Continents are formed by the amalgamation of numerous micro-terranes and island arcs, so
12 they have spatially varying lithosphere strengths. The Crème brûlée (CB) model and the Jelly sandwich
13 (JS) model have been commonly used to describe continental lithosphere strength-depth variations.
14 Depending on the strength of continental lower crust, the CB and JS models can be further subdivided
15 into two subclasses, in which the I subclass (CB-I and JS-I) and II subclass (CB-II and JS-II)
16 respectively have a strong or weak lower crust. During continental collision, lithosphere deformation is
17 the byproduct of the comprehensive interaction of multiple terranes. Here we used 2-D
18 thermo-mechanical numerical models that contain three continental terranes to systematically explore
19 the effects of terranes with various strengths on continental deformation, and studied the effects of
20 different rheological assumptions terrane deformation. We find four types of lithosphere deformation
21 patterns: collision, subduction, thickening and delamination, and replacement. Lithosphere structures,
22 especially local pre-existing weaknesses, also have nonnegligible influences on lithosphere
23 deformation. These simulation patterns are seen in observed deformation patterns and structures in East
24 Asia, suggesting they are likely to be naturally occurring modes of intracontinental orogenesis.

25 **1. Introduction**

26 Continents have undergone multiple break-up and assembly events during the past ~2 billion years,
27 with the assembly events often being associated with the accretion and deformation of numerous
28 micro-terranes (Mitchell et al., 2021). Accreted terranes have different ages ranging from ~3500 – 3000



29 Ma to 50 – 0 Ma, and diverse compositions and structures linked to their diverse continental, arc, or
30 oceanic origin, which often leads to them having distinct initial lithospheric thicknesses and strengths
31 (Artemieva, 2006; Audet and Bürgmann, 2011; Pasyanos et al., 2014; Morgan and Vannucchi, 2022).
32 The lithosphere of ancient continental terranes like cratons are usually thick and strong, while younger
33 lithosphere of continental margins and tectonically active regions is thin and weak (Audet and
34 Bürgmann, 2011; Burov, 2011), and deeply buried former oceanic fragments can have temperature and
35 strengths that vary over ~0.5 Gyr timescale (Morgan and Vannucchi, 2022).
36 Continental lithosphere strength conventionally been represented by two prevailing rheology models
37 —the Crème brûlée (CB) and the Jelly sandwich (JS) idealizations (Chen and Molnar, 1983; Jackson,
38 2002; Burov and Watts, 2006; Bürgmann and Dresen, 2008; Burov, 2011). The Crème brûlée scenario
39 suggests that lithosphere strength resides entirely in the crust, with the lithospheric mantle being much
40 weaker (with this strength contrast being the explanation for why little seismicity is typically seen in
41 the continental mantle, despite rock-mechanics arguments that it should usually be stronger than its
42 overlying crust). In contrast, the Jelly sandwich model is based on conventional rock mechanics
43 arguments which imply that in general the continental middle and lower crust should be weaker than
44 overlying cooler upper crust and underlying further-from-solidus lithospheric mantle (Figure 1a). The
45 rheology of the continental lower crust can also differ strongly in different continental terranes due to
46 the varieties in composition, temperature, water content, stress, and tectonic environment (Bürgmann
47 and Dresen, 2008; Hacker et al., 2015; Morgan and Vannucchi, 2022). Therefore, the CB and JS
48 conceptualizations can be further subdivided into CB-I and CB-II, JS-I, and JS-II subclasses that reflect
49 potentially variable strengths of the lower crust: CB-I and JS-I, CB-II and JS-II have strong and weak
50 continental lower crust, respectively (Fig. 1a). Observations in Eastern Asia show a wide variability in
51 terrane deformation styles that argue for the potential feasibility of all four of these rheological models
52 (Figure 1b; Zhang et al., 2013).
53 Several previous numerical modelling studies have discussed the effects of rheological contrasts
54 between terranes in lithosphere deformation in a collisional system. Studies containing two terranes
55 have explored contrasts in crustal rheology, and found that this can greatly change the morphology, size
56 and deep lithosphere structure of collisional orogenic belt (Chen, 2021; Chen et al., 2017; Cook and
57 Royden, 2008; Faccenda et al., 2008; Sun and Liu, 2018; Vogt et al., 2018; Xie et al., 2021). Strong
58 crust also has the potential to protect its underlying lithospheric mantle from deformation and



59 destruction (Heron and Pysklywec, 2016). Studies containing three or more terranes in their models
60 have usually focused on the middle terrane which can play a crucial role in lithosphere deformation in a
61 collisional system (Kelly et al., 2016, 2020; Li et al., 2016; Huangfu et al., 2018, 2022; Sun and Liu,
62 2018; Xie et al., 2023). A weak middle terrane is easy to be thickened, to the point where eventually its
63 lithospheric mantle can be delaminated from the crust; while a moderate-strength middle terrane can
64 induce far-field orogenesis; and a strong middle terrane may prevent propagation of deformation and
65 facilitate underthrusting of the advancing terrane. In addition, some studies have also stressed the
66 importance of local pre-existing weak zones which can change the order and style of lithosphere
67 deformation (Chen et al., 2020; Heron et al., 2016; Sokoutis and Willingshofer, 2011; Xie et al., 2021).
68 In modern Asia, the large-scale Alpine-Himalaya continental collisional system often involves the
69 multiple units of an indenting terrane, a middle terrane, and far-end backwall terranes. The different
70 lithosphere rheologies of these terranes collectively contribute to several styles of continental
71 deformation. Here, we use a 2-D thermo-mechanical numerical modeling method to systematically
72 study the effects of terranes with various rheological properties on continental deformation. Our
73 numerical models simulate a continent-continent collisional system that contains three continental
74 terranes. It explores the effects of four groups of lithosphere deformation patterns linked to the four
75 rheological idealizations of CB-I, CB-II, JS-I, and JS-II applied to each terrane. We will summarize the
76 rheological features for each deformation pattern, and then apply the simulations to better understand
77 ongoing and past deformation histories preserved in eastern Eurasia.

78 **2. Numerical modelling method and model setup**

79 **2.1. Numerical modelling method**

80 Our thermo-mechanical models were performed with the I2VIS code of Gerya and Yuen (2003),
81 previously used in Xie et al. (2021, 2023). This code combines finite differences with marker-in-cell
82 techniques to solve the mass, momentum, and energy conservation equations for incompressible flow.
83 It incorporates the non-Newtonian visco-plastic rheologies for the lithosphere, as well as the possibility
84 to include parameterizations of the effects of surface processes like sedimentation and erosion.

85 **2.1.1. Governing equations**

86 The mass conservation equation for incompressible flow is:



$$87 \quad \frac{\partial v_x}{\partial x} + \frac{\partial v_y}{\partial y} = 0, \quad (1)$$

88 The momentum conservation equations (Stokes equations) are:

$$89 \quad \begin{aligned} \frac{\partial \sigma'_{xx}}{\partial x} + \frac{\partial \sigma'_{xy}}{\partial y} &= \frac{\partial P}{\partial x}, \\ \frac{\partial \sigma'_{yy}}{\partial y} + \frac{\partial \sigma'_{xy}}{\partial x} &= \frac{\partial P}{\partial y} - g\rho \end{aligned} \quad (2)$$

90 The energy (heat) conservation equation is:

$$91 \quad \begin{aligned} \rho C_p \frac{DT}{Dt} &= -\frac{\partial q_x}{\partial x} - \frac{\partial q_y}{\partial y} + H_r + H_s + H_a + H_L \\ q_x &= -k \frac{\partial T}{\partial x} \\ q_y &= -k \frac{\partial T}{\partial y} \\ H_a &= T\alpha \frac{DP}{Dt} \\ H_s &= \sigma'_{xx} \dot{\epsilon}_{xx} + \sigma'_{yy} \dot{\epsilon}_{yy} + 2\sigma'_{xy} \dot{\epsilon}_{xy} \end{aligned} \quad (3)$$

92 where x and y represent the horizontal and vertical coordinate directions, and v_x and v_y are the
 93 corresponding velocity components, respectively. σ'_{ij} and $\dot{\epsilon}_{ij}$ ($i, j = x, y$) are deviatoric stress and
 94 strain-rate tensors, respectively; g is the gravitational acceleration; ρ is density. In the heat conservation
 95 equation, q_x and q_y are the horizontal and vertical components of the heat flux, respectively; C_p is heat
 96 capacity, and H_r , H_a , H_s , and H_L denote the radioactive, adiabatic, shear, and latent heat production,
 97 respectively; k is the thermal conductivity.

98 The rheological constitutive relationship connects the deviatoric stress and strain rate:

$$99 \quad \begin{aligned} \sigma'_{xx} &= 2\eta_{eff} \dot{\epsilon}_{xx}, \quad \dot{\epsilon}_{xx} = \frac{\partial v_x}{\partial x} \\ \sigma'_{xy} &= 2\eta_{eff} \dot{\epsilon}_{xy}, \quad \dot{\epsilon}_{xy} = \frac{1}{2} \left(\frac{\partial v_x}{\partial y} + \frac{\partial v_y}{\partial x} \right), \\ \sigma'_{yy} &= 2\eta_{eff} \dot{\epsilon}_{yy}, \quad \dot{\epsilon}_{yy} = \frac{\partial v_y}{\partial y} \end{aligned} \quad (4)$$

100 where η_{eff} is the effective viscosity.



101 **2.1.2. Rheology**

102 Here we make the conventional assumption that the crust and mantle have a visco-plastic rheology.
 103 Viscous deformation is determined as a combination of diffusion and dislocation creep that depends on
 104 temperature, pressure, and strain rate, expressed as (Gerya, 2019):

$$105 \quad \eta_{disl} = \frac{1}{2} \frac{1}{(A_D)^{-1/n} (\dot{\epsilon}_{II})^{(n-1)/n}} \exp\left(\frac{E_a + V_a P}{nRT}\right) * S, \quad (5)$$

$$\eta_{diff} = \frac{1}{2} \frac{A_D}{\sigma_{cr}^{(n-1)}} \exp\left(\frac{E_a + V_a P}{RT}\right) * S$$

106 For mineral aggregates, both dislocation and diffusion creep occur simultaneously, with a combined
 107 effective viscosity given by:

$$108 \quad \frac{1}{\eta_{ductile}} = \frac{1}{\eta_{disl}} + \frac{1}{\eta_{diff}}, \quad (6)$$

109 where η_{disl} and η_{diff} are viscosities for dislocation and diffusion creep, respectively. σ_{cr} is the
 110 critical stress for the dislocation to diffusion stress transition, and the parameters A_D , E_a , V_a , and n are a
 111 material constant, activation energy, activation volume, and stress exponent, respectively, and R is the
 112 universal gas constant. The strength scaling factor, S , is introduced as a simple parameter to vary the
 113 lithospheric viscosity.

114 Plasticity is implemented using a conventional pseudo-viscous yield criterion first used to study rifting
 115 (e.g. Chen and Morgan, 1990) that is extended to include a strain-weakening-like parameterization of
 116 fracture-related strain weakening (Gerya et al., 2010; Vogt et al., 2017):

$$117 \quad \eta_{plastic} = \frac{\sigma_{yield}}{2\dot{\epsilon}_{II}}$$

$$\sigma_{yield} = C + P\phi$$

$$C = \begin{cases} C_a + (C_b - C_a) \times \frac{\gamma}{\gamma_{cr}}, & \text{if } \gamma \leq \gamma_{cr}, \\ C_b, & \text{if } \gamma \geq \gamma_{cr} \end{cases}, \quad (7)$$

$$\phi = \begin{cases} \phi_a + (\phi_b - \phi_a) \times \frac{\gamma}{\gamma_{cr}}, & \text{if } \gamma \leq \gamma_{cr} \\ \phi_b, & \text{if } \gamma \geq \gamma_{cr} \end{cases}$$

118 where σ_{yield} is yield stress, P is dynamic pressure, γ is the integrated plastic strain, and γ_{cr} is the



119 upper strain limit for fracture-related weakening. C and ϕ are cohesion and friction angle that depend
120 on the plastic value. C_a and ϕ_a are the initial and C_b and ϕ_b are final strength values, respectively.
121 This involves making the rheological assumption that deeply percolating fluids and high pore fluid
122 pressures can significantly lower the plastic strength of fractured rocks.
123 The final effective viscosity is determined by the minimum value between the ductile and plastic
124 viscosities (Ranalli, 1995):

$$125 \quad \eta_{eff} = \min(\eta_{ductile}, \eta_{plastic}). \quad (8)$$

126 2.1.3. Surface processes

127 Topography in our models evolves according to a transport equation that is solved at each time step,
128 with a crude local parameterization of effects of accounts for sedimentation and erosion:

$$129 \quad \frac{\partial y_{es}}{\partial t} = v_y - v_x \frac{\partial y_{es}}{\partial x} - v_s + v_e. \quad (9)$$

130 Where y_{es} is the vertical position of the surface as a function of horizontal distance x ; and v_x and v_y are
131 the corresponding velocity components, respectively; and v_s and v_e are the sedimentation and erosion
132 rates, respectively.

133 2.2. Model Setup

134 The 2-D numerical model covers a rectangular computational domain of 3000 km \times 700 km and
135 consists of 1360 \times 400 non-uniform grids with dozens of mobile markers in each grid to transport
136 physical properties (Figure 2a). Above 300 km, the cell-size of the grid in the middle of model ($X =$
137 1300 – 2200 km) is 1 km \times 1 km, and gradually widens towards the two sides to finally become 5 km \times
138 1 km. From the 300 km depth to the model bottom, each grid is stretched to 5 km in the vertical
139 direction. As a result, the grid in the middle of the model ($X = 1300 – 2200$ km) is 1 km \times 5 km and is
140 5 km \times 5 km in the other regions. Changing resolutions in different model regions can ensure the model
141 can finely depict lithosphere deformation in the region of interest while improving the calculation's
142 efficiency.

143 In the initial configuration, the model comprises three continental terranes — the Pro-, Mid- and
144 Retro-terrane — which refer to the indenting 'Pro-' terrane driven by plate convergence, an



145 intermediate ‘Mid-’ terrane, and a far-end backwall ‘Retro-’ terrane, respectively (Figure 2a). The three
146 terranes are assumed to have the same initial crustal structure with 20 km upper and lower crust,
147 respectively. Thicknesses of the initial lithospheric mantle of the Pro-, Mid- and Retro-terrane are 160
148 km, 90 km, and 120 km, respectively. Variable lithosphere thicknesses for the Pro-, Mid- and
149 Retro-terranes simulate lateral structure differences within continental lithosphere (Pasyanos et al.,
150 2014). The rest of the region is filled by asthenosphere except along the model top, where a 20 km
151 thick layer of “sticky air” with low viscosity (1×10^{18} Pas) and low density (1 kg/m^3) is placed to
152 simulate the effects of a free surface (Schmeling et al., 2008). Flow laws and material properties for
153 each lithospheric layer are listed in Table 1.

154 Mechanical boundary conditions of the model are that the top and sides are free-slip boundaries, and
155 the bottom is assumed to be a somewhat non-physical ‘permeable boundary’ that was developed to
156 reduce the required depth of the computational region (Burg and Gerya, 2005). For top-driven flows
157 like those considered here, this approximation has been shown to not affect deformation in the upper
158 parts of the region (Burg and Gerya, 2005). Initial temperature conditions are set as follows: the model
159 top is set to at 0°C , the two side boundaries are adiabatic boundaries with zero horizontal heat fluxes,
160 and the model bottom has an initial temperature of 1593°C , and can dynamically adjust as the model
161 evolves. The initial thermal gradient in the crust is 15°C/km in the three terranes, so their Moho
162 temperature is 600°C . A temperature of 1330°C is applied at the bottom of the lithospheric mantle of
163 the three terranes, which leads to the Pro- and Mid-terrane having minimum and maximal thermal
164 gradients in the lithospheric mantle, respectively (see the right plane in Figure 2a). An adiabatic
165 thermal gradient of 0.5°C/km is assumed within the asthenosphere. The initial setup of lithosphere
166 structure and temperature field make the Mid-terrane weakest when same rheology model is used for
167 the three terranes. Finally, a constant convergence rate of 20 mm/yr is assigned to the Pro-terrane ($X =$
168 1000 km) to drive the model.

169 3. Simulation Results

170 The rheological models of CB-I, CB-II, JS-I, and JS-II assume different strength scaling factors for the
171 upper crust, the lower crust, and the lithospheric mantle (Figure 2b). We systematically test the effects
172 of these rheological assumptions on the deformation of the Pro-, Mid- and Retro-terranes. Simulation



173 results can be categorized into four basic modes of lithosphere deformation: collision, subduction,
174 thickening and delamination, and replacement (Figure S1). We select a typical case for each mode of
175 lithosphere deformation to discuss more details of these modes of model evolution.

176 **3.1. Case 1: Lithosphere Collision**

177 Case 1 represents the scenario of lithosphere collision between the Pro- and Retro-terrane (Figure 3).
178 In this model, the assumed rheological models for the Pro-, Mid- and Retro-terrane are JS-I, JS-II, and
179 JS-I, respectively, which means that the Mid-terrane has a significantly weaker lower crust relative to
180 the Pro- and Retro-terrane. The lithospheric mantle of the Mid-terrane is also slightly weaker due to its
181 thinner lithosphere and correspondingly higher initial temperature field. Strength profiles on the right
182 top of Fig. 3 show the lithosphere strengths of the three terranes.

183 The Mid-terrane is the first to deform when the Pro-terrane begins to collide, absorbing plate
184 convergence in the form of lithosphere thickening. The upper crust of the Mid-terrane breaks due to
185 strain weakening, and several reverse faults with opposite dip directions form to absorb crustal
186 shortening. The lower crust folds, and strain diffusely distributes within it. Since the Retro-terrane is
187 relatively strong, it prevents crustal deformation from propagating into this terrane, and restricts the
188 bulk of deformation to the Mid-terrane. With continuous advance of the Pro-terrane and resistance of
189 the Retro-terrane, the crust of the Mid-terrane is intensively shortened, leading to more thrusting
190 structures in the upper crust and a “flower-like” structure in the lower crust. Thrust structures and
191 crustal deformation also expand toward the Pro- and Retro-terrane at this stage. Topography also
192 grows towards the two bounding terranes (Figure 7a). Ultimately, the weak lithospheric mantle of the
193 Mid-terrane is squeezed out, and the Pro- and Retro-terrane's lithospheric mantles meet and so start to
194 collide beneath the overlying crust of the Mid-terrane.

195 Crustal deformation and topographic uplift first occur in the middle terrane, then expand towards the
196 bounding terranes. Ultimately, the lithospheric mantles of the bounding terranes begin to collide after
197 extruding/removing the lithospheric mantle beneath the middle terrane.

198 **3.2. Case 2: Lithosphere Subduction**

199 Case 2 shows lithosphere subduction of the Pro-terrane (Figure 4). In this model, the assumed
200 rheological models for the Pro-, Mid- and Retro-terrane are JS-II, JS-I, and JS-I, respectively. The



201 Mid-terrane has a stronger lower crust and weaker lithospheric mantle than the Pro-terrane (see the
202 strength profiles on the right top of Figure 4). When convergence begins, the weak lower crust of the
203 Pro-terrane is blocked by the stronger lower crust of the Mid-terrane. This induces it to stack in a
204 collisional front to form a remarkable folding structure. The strong lithospheric mantle of the
205 Pro-terrane continues to move forward and underthrusts beneath the Mid-terrane. As the Pro-terrane
206 advances, its crust gradually enters the Mid-terrane, inducing shortening and thickening of the upper
207 crust of the Mid-terrane.

208 Meanwhile, the lithospheric mantle of the Pro-terrane continues to underthrust and scrapes off part of
209 the lithospheric mantle of the Mid-terrane. Eventually, the crust of the Pro-terrane wedges a long
210 distance into the Mid-terrane, and the lithospheric mantle of the Pro-terrane subducts into the deeper
211 mantle. In this example, crustal deformation and topography gradually propagate from the Pro-terrane
212 to the Mid-terrane, whereas the Retro-terrane remains nominally ‘undeformed’ at all times (Figure 7b).
213 In some experiments, the lithospheric mantle of the Retro-terrane can subduct beneath the Mid-terrane
214 (Figure S1). In this deformation pattern, (1) crustal deformation and topography gradually propagates
215 from one of the bounding terranes into the other bounding terrane through the middle terrane, and (2)
216 the lithospheric mantle of bounding terrane subducts into the deep mantle beneath the middle terrane.

217 **3.3. Case 3: Lithosphere Thickening and Delamination**

218 Case 3 illustrates the thickening and delamination of the lithospheric mantle of the Pro-terrane (Figure
219 5). In this case, the rheological models for the Pro-, Mid- and Retro-terrane are CB-II, JS-I, and JS-I,
220 respectively. The Pro-terrane has a more fragile lower crust and lithospheric mantle, making it
221 relatively easy to deform once the collision has started. The lithospheric mantle of the Pro-terrane is
222 first shortened and thickened, in which leads to crustal folding. The lower part of the thickened
223 lithospheric mantle is denser than its ambient mantle, which causes it to drip downwards. After
224 delamination of the thickened lithosphere, subduction initiation occurs within the lithospheric mantle of
225 the Pro-terrane. Crustal deformation is restricted in the Mid-terrane until lithosphere delamination, after
226 which crustal strain and topography rapidly spread from the Pro-terrane to the Mid-terrane (Fig. 7c).
227 Like case 2, the Retro-terrane stays essentially undeformed at all times.

228 If the lithosphere of the Pro- or Retro-terrane is extremely weak, for example, its rheology model is
229 CB-II, then lithosphere thickening and delamination may occur. In this deformation pattern, (1) the



230 weak lithosphere of the bounding terrane first thickens by compression and then delaminates due to its
231 density, while (2) crustal deformation rapidly propagates from the thickened bounding terrane into the
232 middle terrane following lithosphere delamination.

233 **3.4. Case 4: Lithosphere Replacement**

234 Case 4 illustrates how the lithospheric mantle of the Pro-terrane can be replaced by that of a
235 neighboring stronger Mid-terrane (Figure 6). In this case, the rheological models for the Pro-, Mid- and
236 Retro-terrane are CB-I, JS-II, and JS-I, respectively. The Pro-terrane has a strong lower crust and a
237 thick and weak lithospheric mantle, while the Mid-terrane has a weaker lower crust and a strong
238 lithospheric mantle. This lithosphere configuration between the Pro- and the Mid-terrane causes
239 deformation to be primarily distributed in the Pro-terrane's lithospheric mantle and the Mid-terrane's
240 crust. As a result, the Mid-terrane's crust becomes intensely shortened by fold and thrust structures, but
241 its strong lithospheric mantle wedges into the Pro-terrane's thick and weak lithospheric mantle. The
242 strong lithospheric mantle of the Mid-terrane scrapes off the lower part of the weak lithospheric mantle
243 of the Pro-terrane and so replaces it. Similar to case 1, crustal deformation and topography expand
244 from the Mid-terrane towards its side terranes (Figure 7d).

245 The lithospheric mantle of the Retro-terrane can also be replaced in some cases (e.g. Figure S1). In this
246 deformation pattern, the significant deformation features are that: (1) part of the weak lithospheric
247 mantle of the bounding terrane is replaced by the strong lithospheric mantle of the middle terrane; (2)
248 crustal deformation and topography expand from center towards the two sides.

249 **4. Discussion**

250 **4.1. Rheological Characteristics for Distinct Lithosphere Deformation Patterns**

251 Distinct lithosphere deformation patterns in our simulation results result from rheological contrasts
252 between neighboring continental terranes. Figure 8 summarizes the rheological characteristics of these
253 distinct deformation patterns (Figure 8). When the Mid-terrane's mantle is weakest (typified by models
254 in which the rheological model of the Mid-terrane is CB-II), it is easy for its mantle to be extruded,
255 leading to collision between the lithospheric mantles of its surrounding Pro- and Retro-terrane. When
256 the Pro- or Retro-terrane's mantle is weakest, its lithosphere is first to be thickened by compression and
257 then delaminated due to the resulting density-driven instability. When the lower crust of the



258 Mid-terrane is relatively strong (CB-I or JS-I), while it is weaker in the Pro- or Retro-terrane (CB-II or
259 JS-II), then the lithospheric mantle of the Pro- or Retro-terrane will tend to subduct into the deep
260 mantle, e.g. leading to intracontinental subduction. Finally, when the Mid-terrane has a weak lower
261 crust and strong lithospheric mantle (JS-II), while the Pro- or Retro-terrane has a strong lower crust and
262 lithospheric mantle (CB-I), then the lithospheric mantle of the former replaces the lithospheric mantle
263 of the latter.

264 In the deformation patterns involve the collision and replacement of lithosphere, continental
265 deformation involves all three terranes (Figures 3 and 6). In contrast, the other deformation patterns
266 only involve two terranes, the Pro-or Retro-terrane and the Mid-terrane (Figures 4 and 5). The
267 rheological properties of the Mid-terrane are responsible for these differences. Like previous numerical
268 studies (Kelly et al., 2016, 2020; Li et al., 2016; Huangfu et al., 2018, 2022; Sun and Liu, 2018), our
269 simulations show that weak a Mid-terrane is easier to deform, and that in this case lithosphere
270 deformation will expand from center to its neighboring sides; while a relatively strong Mid-terrane
271 prevents deformation from propagating far, so that lithosphere deformation is constrained to occur
272 within two terranes. The simulation results also highlight the potential effects of differences in
273 rheological stratification between different terranes to lithosphere deformation (Figures 4 and 6).

274 **4.2. Influence of Lithosphere Structure**

275 Lithospheric thickness is one of the critical factors that controls its strength (Burov, 2011); this can
276 strongly vary between tectonic regions (Pasyanos et al., 2014). In our models, we assume different
277 lithospheric thicknesses for the Pro-, Mid- and Retro-terrane to explore these effects. Complex effects
278 are seen. When changing the lithospheric thicknesses of the Mid-terrane, or of all three terranes,
279 remarkable variations in lithosphere deformation appear in cases 1 and 2, but smaller variations are
280 seen for cases 3 and 4 (Figure 9). Cases 1 and 2 assume a Jelly sandwich rheology for the Pro-, Mid-
281 and Retro-terrane, so the strength of lithospheric mantle of three terranes is comparable. Strength
282 variations produced by differences in lithospheric thickness may alter the relative strength of the three
283 terranes, resulting in distinct lithospheric deformations. Instead, in cases 3 and 4, the Pro-, Mid- and
284 Retro-terrane have two regions with stronger Jelly-sandwich-like rheological structures and one with a
285 weaker Crème brûlée structure, and deformation preferentially concentrates in the weaker terrane with
286 a weak mantle Crème brûlée rheology. In comparison to the large strength difference implied for the



287 lithospheric mantle between the Crème brûlée and Jelly Sandwich rheological models, the strength
288 variations associated with the differences in lithosphere thickness are relatively small. Therefore,
289 changing the thicknesses of the lithosphere has much smaller effects on the lithosphere deformation, as
290 seen in cases 3 and 4.

291 In addition, the weak zones that suture two terranes are generally preserved during continental
292 amalgamation (Burker et al., 1977; Vink et al., 1984; Yin and Harrison, 2000). These local pre-existing
293 lithosphere weaknesses would be preferentially activated if the continental lithosphere were subjected
294 to compression, and could play a key role in concentrating deformation, adjusting deformation
295 sequences, and inducing lithosphere subduction (Sokoutis and Willingshofer, 2011; Heron et al., 2016;
296 Chen et al., 2020; Xie et al., 2021, 2023). Comparing the simulation results of models with and without
297 weak zone, we find that a weak zone will facilitate lithosphere subduction in earlier stages of model
298 evolution, resulting in more diverse lithosphere deformation patterns during the later stage (Figure S2).

299 **4.3. Implications for the Tectonics of Eurasia**

300 The eastern Tien Shan is an ideal region to study the deformation patterns linked to long-term
301 lithosphere collision. The eastern Tien Shan is located east of the geographic longitude of 80° E and is
302 bounded by the Tarim Basin to the south, and the Junggar Basin to the north (Figure 10a). It is
303 composed of a series of former island arcs and small continental blocks that amalgamated during the
304 late Paleozoic (Han and Zhao, 2017). The lithosphere of the eastern Tien Shan is weaker and thinner in
305 comparison to its neighboring Tarim Basin and Junggar Basin (Kumar et al., 2005; Lei and Zhao et
306 al., 2007; Zhang et al., 2013; Deng and Tesauro, 2016). At ~20 – 25 Ma, the eastern Tien Shan became
307 a reactivated orogeny in response to ongoing India-Asia collision (Yin et al., 1998). Compression
308 linked to the India-Asia collision induced the Tarim lithosphere to underthrust northward (Xu et al.,
309 2002; Guo et al., 2006; Lei and Zhao et al., 2007; Lü et al., 2019; Hapaer et al., 2022; Sun et al., 2022).
310 In the northern part of the eastern Tien Shan, significant high-velocity anomalies and Moho overlap are
311 also imaged, which are conventionally explained as being due to the southward underthrusting of the
312 Junggar lithosphere (Xu et al., 2002; Guo et al., 2006; Li et al., 2016; Lü et al., 2019). High-velocity
313 anomalies in the Tarim and Junggar lithosphere appear to connect beneath the eastern Tien Shan,
314 suggesting the lithosphere of the Tarim and Junggar Basins has converged and collided together in this
315 region (Figure 10b and 11c; Lü et al., 2019). Bidirectional underthrusting of the Tarim and Junggar



316 lithosphere leads to intense crustal shortening and thrust faults on both flanks over the adjacent basins,
317 as well as attendant fold and reverse fault zones along the range fronts (Yin et al., 1998; Wang et al.,
318 2004).

319 The deformation pattern arising from lithosphere thickening and delamination has been applied to the
320 Tibetan Plateau. Tibetan lithosphere may have been significantly weakened by hydration,
321 metasomatism, and partial melting of the lithospheric mantle during a series of oceanic closure and
322 terrane accretion events before the India-Asia collision (Yin and Harrison, 2000; Zhang et al., 2014;
323 Ma et al., 2021). It was then pushed northward by the Indian craton and was blocked by the
324 Tarim/Qaidam craton during India-Asia collision, leading to double crustal thickness (Zhao and
325 Morgan, 1985; Zhang et al., 2011). The lithosphere beneath the Tibetan Plateau does not thicken
326 significantly like its crust, especially beneath northern Tibet (Owens and Zandt, 1997; Tunini et al.,
327 2016). Numerous observations instead suggest that the Tibetan lithosphere has been detached from the
328 crust and has sunk into deeper mantle, consistent with the presence of high-velocity regions in the deep
329 mantle in western, southern and southeastern Tibet (Li et al., 2008; Chen et al., 2017; Feng et al., 2021).
330 A significant depression of the 660-km discontinuity beneath the Himalaya terrane and the uplift of
331 410-km discontinuity in western Tibet have also attributed to the presence of delaminated Tibetan
332 lithosphere (Wu et al., 2022). In northern Tibet, anomalously high temperatures are assumed to be
333 linked to a region of inefficient Sn propagation, while a remarkable low-velocity zone in the mantle
334 and ultra-potassic volcanics also suggest lithosphere thinning (Barazangi and Ni, 1982; Turner et al.,
335 1996; Owens and Zandt, 1997; Guo et al., 2006; Liang et al., 2012; Tunini et al., 2016). After
336 lithosphere thinning commenced in the Miocene, the Tibetan Plateau rapidly grew outwards rapidly
337 (Lu et al., 2018 and references therein; Molnar et al., 1993; Xie et al., 2023).

338 An example of intracontinental subduction is the Early Paleozoic Orogen in Southeastern China which
339 appears to have not been preceded by oceanic subduction (Faure et al., 2009). The Early Paleozoic
340 Orogen of Southeastern China is located on the Wuyi-Yunkai Fold Belt. Arguments against it being a
341 collisional orogenic belt are its lack of preserved ophiolites, a magmatic arc, subduction complexes,
342 and high-pressure metamorphism. Instead, structural, metamorphic, and sedimentary elements indicate
343 that this orogen was an intracontinental orogen controlled by the northward subduction of Cathaysia
344 (Faure et al., 2009). A weak suture/failure zone inherited from previous tectonic events contributed to
345 the internal subduction of Cathaysia, during which ductile decollements accommodated horizontal



346 shortening by folding and thrusting. The tectonic development of this orogen appears similar to the
347 deformation mode of lithosphere subduction (Figure 4).

348 So far, we have yet to find a suitable region to apply the model deformation pattern of lithosphere
349 replacement. In this deformation pattern, crustal deformation and topographic evolution are similar to
350 those in the deformation pattern of lithosphere collision (Figures 7a and 7c). Thus, it is not easy to
351 identify this pattern by geological and geophysical techniques when the replaced and original
352 continental lithosphere has similar properties. Improved imaging observations with better resolution
353 may allow this deformation pattern to be identified in the future.

354 5. Conclusions

355 The continental lithosphere is likely to have strong lateral variations in its strength. We explored 2-D
356 numerical models that contain three diverse types of continental terranes to study the responses of
357 continental terranes with different strengths to compression. Four rheological models were respectively
358 applied to each of the Pro-, Mid- and Retro-terrane, and simulation results can be grouped into four
359 distinct deformation styles: lithosphere collision, subduction, thickening and delamination, and
360 replacement. These deformation styles arise from the rheological contrasts between these terranes: (1)
361 when the middle terrane is the weakest, its lithosphere is easily extruded, which leads to lithosphere
362 collision between its two bounding terranes; (2) when the middle terrane has a strong lower crust, while
363 the lower crust of a bounding terrane is weak, then subduction of the lithosphere of the bounding
364 terrane will occur; (3) when a bounding terrane is the weakest, its lithosphere would tend to be
365 thickened by lateral compression, followed by lithosphere delamination due to the resulting
366 density/gravitational instability; (4) when a bounding terrane has a strong lower crust and weak
367 lithospheric mantle, while the middle terrane has a weak lower crust and strong lithospheric mantle,
368 then lithosphere replacement will again occur. These simulation patterns are seen in observed
369 deformation patterns and structures in the eastern Tien Shan, and the Tibetan Plateau, the Early
370 Paleozoic Orogen of Southeastern China, suggesting they are likely to be naturally occurring modes of
371 intracontinental orogenesis.



372 **Code availability**

373 Requests for the numerical code I2VIS should be sent to the main developer
374 (taras.gerya@erdw.ethz.ch).

375 **Data availability**

376 Numerical modeling data are provided in Zenodo (<https://doi.org/10.5281/zenodo.8354366>).

377 **Author contribution: Conceptualization:** Yongshun John Chen; **Methodology:** Lin Chen, Renxian
378 Xie; **Investigation:** Renxian Xie; **Formal analysis:** Renxian Xie, Lin Chen; **Visualization:** Renxian
379 Xie, Jason P. Morgan; **Writing – original draft preparation:** Renxian Xie; **Funding acquisition:**
380 Yongshun John Chen, Lin Chen.

381 **Competing interests:** The authors declare that they have no conflict of interest.

382 **Disclaimer. Publisher's note:** Copernicus Publications remains neutral with regard to jurisdictional
383 claims in published maps and institutional affiliations.

384 **Acknowledgments**

385 The authors sincerely thank Prof. Taras Gerya for providing the I2VIS package and his long-lasting
386 guidance on our geodynamic modeling. The authors acknowledge that figures of simulation results
387 were prepared with the Generic Mapping Tools (GMT, <http://www.soest.hawaii.edu/gmt/>). All models
388 were performed on the TianHe-1A system at the National Supercomputer Center in Tianjin.

389 **Financial support:** This study was supported by the National Natural Science Foundation of China
390 (Grants U1901602) and the National Key R&D Program of China (2022YFF0800800).

391 **References**

392 Artemieva, I. M.: Global 1×1 thermal model TC1 for the continental lithosphere: implications for
393 lithosphere secular evolution, *Tectonophysics*, 416, 245-277,



- 394 <https://doi.org/10.1016/j.tecto.2005.11.022>, 2006.
- 395 Audet, P., and Bürgmann, R.: Dominant role of tectonic inheritance in supercontinent cycles, *Nature*
396 *geoscience*, 4, 184-187, <https://doi.org/10.1038/ngeo1080>, 2011.
- 397 Barazangi, M., and Ni, J.: Velocities and propagation characteristics of Pn and Sn beneath the
398 Himalayan arc and Tibetan plateau: Possible evidence for underthrusting of Indian continental
399 lithosphere beneath Tibet, *Geology*, 10, 179-185,
400 [https://doi.org/10.1130/0091-7613\(1982\)10<179:VAPCOP>2.0.CO;2](https://doi.org/10.1130/0091-7613(1982)10<179:VAPCOP>2.0.CO;2), 1982.
- 401 Burg, J. P., and Gerya, T. V.: The role of viscous heating in Barrovian metamorphism of collisional
402 orogens: thermomechanical models and application to the Lepontine Dome in the Central Alps,
403 *Journal of Metamorphic Geology*, 23, 75-95, <https://doi.org/10.1111/j.1525-1314.2005.00563.x>,
404 2005.
- 405 Burke, K., Dewey, J. F., and Kidd, W. S. F.: World distribution of sutures—the sites of former oceans,
406 *Tectonophysics*, 40, 69-99, [https://doi.org/10.1016/0040-1951\(77\)90030-0](https://doi.org/10.1016/0040-1951(77)90030-0), 1977.
- 407 Burov, E. B., and Watts, A. B.: The long-term strength of continental lithosphere: "jelly sandwich" or "
408 crème brûlée"? *GSA today*, 16, 4, , doi: 10.1130/1052-5173(2006)016<4:tltSOc>2.0.cO;2, 1997,
409 2006.
- 410 Burov, E. B.: Rheology and strength of the lithosphere, *Marine and petroleum Geology*, 28, 1402-1443,
411 <https://doi.org/10.1016/j.marpetgeo.2011.05.008>, 2011.
- 412 Bürgmann, R., and Dresen, G.: Rheology of the lower crust and upper mantle: Evidence from rock
413 mechanics, geodesy, and field observations, *Annu. Rev. Earth Planet. Sci.*, 36, 531-567, doi:
414 10.1146/annurev.earth.36.031207.124326, 2008.
- 415 Chen, M., Niu, F., Tromp, J., Lenardic, A., Lee, C. T. A., Cao, W., and Ribeiro, J.: Lithospheric
416 foundering and underthrusting imaged beneath Tibet, *Nature communications*, 8, 15659,
417 <https://doi.org/10.1038/ncomms15659>, 2017.
- 418 Chen, L.: The role of lower crustal rheology in lithospheric delamination during orogeny, *Frontiers in*
419 *Earth Science*, 9, 755519, doi: 10.3389/feart.2021.755519, 2021.
- 420 Chen, L., Capitanio, F. A., Liu, L., and Gerya, T. V.: Crustal rheology controls on the Tibetan plateau
421 formation during India-Asia convergence, *Nature Communications*, 8, 15992,
422 <https://doi.org/10.1038/ncomms15992>, 2017.
- 423 Chen, L., Liu, L., Capitanio, F. A., Gerya, T. V., and Li, Y.: The role of pre-existing weak zones in the



- 424 formation of the Himalaya and Tibetan plateau: 3-D thermomechanical modelling, *Geophysical*
425 *Journal International*, 221, 1971-1983, doi: 10.1093/gji/ggaa125, 2020.
- 426 Chen, W. P., and Molnar, P.: Focal depths of intracontinental and intraplate earthquakes and their
427 implications for the thermal and mechanical properties of the lithosphere, *Journal of Geophysical*
428 *Research: Solid Earth*, 88, 4183-4214, <https://doi.org/10.1029/JB088iB05p04183>, 1983.
- 429 Chen Y, Morgan W J.: Rift valley/no rift valley transition at mid-ocean ridges, *Journal of Geophysical*
430 *Research: Solid Earth*, 95(B11): 17571-17581, <https://doi.org/10.1029/JB095iB11p17571>, 1990.
- 431 Cook, K. L., and Royden, L. H.: The role of crustal strength variations in shaping orogenic plateaus,
432 with application to Tibet, *Journal of Geophysical Research: Solid Earth*, 113,
433 <https://doi.org/10.1029/2007JB005457>, 2008.
- 434 Deng, Y., and Tesauro, M.: Lithospheric strength variations in Mainland China: Tectonic implications.
435 *Tectonics*, 35, 2313–2333, <https://doi.org/10.1002/2016TC004272>, 2016.
- 436 Faccenda, M., Gerya, T. V., and Chakraborty, S.: Styles of post-subduction collisional orogeny:
437 Influence of convergence velocity, crustal rheology and radiogenic heat production, *Lithos*, 103,
438 257-287, <https://doi.org/10.1016/j.lithos.2007.09.009>, 2008.
- 439 Faure, M., Shu, L., Wang, B., Charvet, J., Choulet, F., and Monie, P.: Intracontinental subduction: a
440 possible mechanism for the Early Palaeozoic Orogen of SE China, *Terra Nova*, 21, 360-368,
441 <https://doi.org/10.1111/j.1365-3121.2009.00888.x>, 2009.
- 442 Feng, J., Yao, H., Chen, L., and Wang, W.: Massive lithospheric delamination in southeastern Tibet
443 facilitating continental extrusion, *National Science Review*, 9, nwab174, DOI:
444 10.1093/nsr/nwab174, 2022.
- 445 Gerya, T.: Dynamical instability produces transform faults at mid-ocean ridges, *Science*, 329,
446 1047-1050, DOI: 10.1126/science.1191349, 2010.
- 447 Gerya, T.: Introduction to numerical geodynamic modelling, 2nd edition, Cambridge University Press,
448 488pp, ISBN: 9781316534243, <https://doi.org/10.1017/9781316534243>, 2019.
- 449 Gerya, T. V., and Yuen, D. A.: Characteristics-based marker-in-cell method with conservative
450 finite-differences schemes for modeling geological flows with strongly variable transport
451 properties, *Physics of the Earth and Planetary Interiors*, 140, 293-318,
452 <https://doi.org/10.1016/j.pepi.2003.09.006>, 2003.
- 453 Guo, B., LIU, Q. Y., CHEN, J. H., ZHAO, D. P., LI, S. C., and LAI, Y. G.: Seismic tomography of the



- 454 crust and upper mantle structure underneath the Chinese Tianshan, Chinese Journal of Geophysics,
455 49, 1543-1551, <https://doi.org/10.1002/cjg2.982>, 2006.
- 456 Hacker, B. R., Kelemen, P. B., and Behn, M. D.: Continental lower crust, Annual Review of Earth and
457 Planetary Sciences, 43, 167-205, doi: 10.1146/annurev-earth-050212-124117, 2015.
- 458 Han, Y., and Zhao, G.: Final amalgamation of the Tianshan and Junggar orogenic collage in the
459 southwestern Central Asian Orogenic Belt: Constraints on the closure of the Paleo-Asian Ocean,
460 Earth-Science Reviews, 186, 129-152, <https://doi.org/10.1016/j.earscirev.2017.09.012>, 2018.
- 461 Hapaer, T., Tang, Q., Sun, W., Ao, S., Zhao, L., Hu, J., ... and Xiao, W.: Opposite facing dipping
462 structure in the uppermost mantle beneath the central Tien Shan from Pn traveltime tomography,
463 International Journal of Earth Sciences, 111, 2571-2584,
464 <https://doi.org/10.1007/s00531-022-02162-9>, 2022.
- 465 Heron, P. J., and Pysklywec, R. N.: Inherited structure and coupled crust-mantle lithosphere evolution:
466 Numerical models of Central Australia, Geophysical Research Letters, 43, 4962-4970,
467 <https://doi.org/10.1002/2016GL068562>, 2016.
- 468 Heron, P. J., Pysklywec, R. N., and Stephenson, R.: Lasting mantle scars lead to perennial plate
469 tectonics, Nature communications, 7, 11834, <https://doi.org/10.1038/ncomms11834>, 2016.
- 470 Huangfu, P., Li, Z. H., Gerya, T., Fan, W., Zhang, K. J., Zhang, H., and Shi, Y.: Multi-terrane structure
471 controls the contrasting lithospheric evolution beneath the western and central–eastern Tibetan
472 plateau, Nature Communications, 9, 3780, <https://doi.org/10.1038/s41467-018-06233-x>, 2018.
- 473 Huangfu, P., Li, Z. H., Fan, W., Zhang, K. J., and Shi, Y.: Contrasting collision-induced far-field
474 orogenesis controlled by thermo-rheological properties of the composite terrane, Gondwana
475 Research, 103, 404-423, <https://doi.org/10.1016/j.gr.2021.10.020>, 2022.
- 476 Jackson, J. A.: Strength of the continental lithosphere: time to abandon the jelly sandwich?, GSA today,
477 12, 4-10, DOI: 10.1130/1052-5173(2002)012<0004:SOTCLT>2.0.CO;2, 2002.
- 478 Junmeng, Z., Guodong, L., Zaoxun, L., Xiankang, Z., and Guoze, Z.: Lithospheric structure and
479 dynamic processes of the Tianshan orogenic belt and the Junggar basin, Tectonophysics, 376,
480 199-239, <https://doi.org/10.1016/j.tecto.2003.07.001>, 2003.
- 481 Kelly, S., Butler, J. P., and Beaumont, C.: Continental collision with a sandwiched accreted terrane:
482 Insights into Himalayan–Tibetan lithospheric mantle tectonics?, Earth and Planetary Science
483 Letters, 455, 176-195, <https://doi.org/10.1016/j.epsl.2016.08.039>, 2016.



- 484 Kelly, S., Beaumont, C., and Butler, J. P.: Inherited terrane properties explain enigmatic post-collisional
485 Himalayan-Tibetan evolution, *Geology*, 48, 8-14, <https://doi.org/10.1130/G46701.1>, 2020.
- 486 Kumar, P., Yuan, X., Kind, R., and Kosarev, G.: The lithosphere-asthenosphere boundary in the Tien
487 Shan-Karakoram region from S receiver functions: Evidence for continental subduction,
488 *Geophysical Research Letters*, 32, <https://doi.org/10.1029/2004GL022291>, 2005.
- 489 Lei, J., and Zhao, D.: Teleseismic P-wave tomography and the upper mantle structure of the central
490 Tien Shan orogenic belt, *Physics of the Earth and Planetary Interiors*, 162, 165-185,
491 <https://doi.org/10.1016/j.pepi.2007.04.010>, 2007.
- 492 Li, C., Van der Hilst, R. D., Meltzer, A. S., and Engdahl, E. R.: Subduction of the Indian lithosphere
493 beneath the Tibetan Plateau and Burma, *Earth and Planetary Science Letters*, 274, 157-168,
494 <https://doi.org/10.1016/j.epsl.2008.07.016>, 2008.
- 495 Li, J., Zhang, J., Zhao, X., Jiang, M., Li, Y., Zhu, Z., ... and Yang, T.: Mantle subduction and uplift of
496 intracontinental mountains: A case study from the Chinese Tianshan Mountains within Eurasia,
497 *Scientific Reports*, 6, 28831, <https://doi.org/10.1038/srep28831>, 2016.
- 498 Li, Z. H., Liu, M., and Gerya, T.: Lithosphere delamination in continental collisional orogens: A
499 systematic numerical study, *Journal of Geophysical Research: Solid Earth*, 121, 5186-5211,
500 <https://doi.org/10.1002/2016JB013106>, 2016.
- 501 Liang, X., Sandvol, E., Chen, Y. J., Hearn, T., Ni, J., Klemperer, S., ... & Tilmann, F.: A complex
502 Tibetan upper mantle: A fragmented Indian slab and no south-verging subduction of Eurasian
503 lithosphere, *Earth and Planetary Science Letters*, 333, 101-111,
504 <https://doi.org/10.1016/j.epsl.2012.03.036>, 2012.
- 505 Lu, H., Tian, X., Yun, K., and Li, H.: Convective removal of the Tibetan Plateau mantle lithosphere by~
506 26 Ma, *Tectonophysics*, 731, 17-34, <https://doi.org/10.1016/j.tecto.2018.03.006>, 2018.
- 507 Lü, Z., Gao, H., Lei, J., Yang, X., Rathnayaka, S., and Li, C.: Crustal and upper mantle structure of the
508 Tien Shan orogenic belt from full-wave ambient noise tomography, *Journal of Geophysical
509 Research: Solid Earth*, 124, 3987-4000, <https://doi.org/10.1029/2019JB017387>, 2019.
- 510 Ma, L., Wang, Q., Kerr, A. C., and Tang, G. J.: Nature of the pre-collisional lithospheric mantle in
511 central Tibet: Insights to Tibetan Plateau uplift, *Lithos*, 388, 106076,
512 <https://doi.org/10.1016/j.lithos.2021.106076>, 2021.
- 513 Mitchell, R. N., Zhang, N., Salminen, J., Liu, Y., Spencer, C. J., Steinberger, B., ... and Li, Z. X. : The



- 514 supercontinent cycle, *Nature Reviews Earth and Environment*, 2, 358-374,
515 <https://doi.org/10.1038/s43017-021-00160-0>, 2021.
- 516 Molnar, P., England, P., and Martinod, J.: Mantle dynamics, uplift of the Tibetan Plateau, and the Indian
517 monsoon, *Reviews of Geophysics*, 31, 357-396, <https://doi.org/10.1029/93RG02030>, 1993.
- 518 Morgan J P, Vannucchi P. : Transmogrification of ocean into continent: implications for continental
519 evolution, *Proceedings of the National Academy of Sciences*, 119(15): e2122694119,
520 <https://doi.org/10.1073/pnas.2122694119>, 2022.Owens, T. J., and Zandt, G.: Implications of
521 crustal property variations for models of Tibetan plateau evolution, *Nature*, 387, 37-43,
522 <https://doi.org/10.1038/387037a0>, 1997.
- 523 Pasyanos, M. E., Masters, T. G., Laske, G., and Ma, Z.: LITHO1. 0: An updated crust and lithospheric
524 model of the Earth, *Journal of Geophysical Research: Solid Earth*, 119, 2153-2173,
525 <https://doi.org/10.1002/2013JB010626>, 2014.
- 526 Ranalli, G.: *Rheology of the Earth*, 2nd Edition, Springer Science and Business Media, 421pp, ISBN
527 0412546701, 1995.
- 528 Schmeling, H., Babeyko, A. Y., Enns, A., Faccenna, C., Funicello, F., Gerya, T., ... and Van Hunen, J.:
529 A benchmark comparison of spontaneous subduction models—Towards a free surface, *Physics of*
530 *the Earth and Planetary Interiors*, 171, 198-223, <https://doi.org/10.1016/j.pepi.2008.06.028>, 2008.
- 531 Sokoutis, D., and Willingshofer, E.: Decoupling during continental collision and intra-plate
532 deformation, *Earth and Planetary Science Letters*, 305, 435-444,
533 <https://doi.org/10.1016/j.epsl.2011.03.028>, 2011.
- 534 Sun, W., Ao, S., Tang, Q., Malusà, M. G., Zhao, L., and Xiao, W.: Forced Cenozoic continental
535 subduction of Tarim craton-like lithosphere below the Tianshan revealed by ambient noise
536 tomography, *Geology*, 50, 1393-1397, <https://doi.org/10.1130/G50510.1>, 2022.
- 537 Sun, Y., and Liu, M.: Rheological control of lateral growth of the Tibetan Plateau: Numerical results,
538 *Journal of Geophysical Research: Solid Earth*, 123, 10-124,
539 <https://doi.org/10.1029/2018JB016601>, 2018.
- 540 Tunini, L., Jimenez-Munt, I., Fernandez, M., Verges, J., Villasenor, A., Melchiorre, M., and Afonso, J.
541 C.: Geophysical-petrological model of the crust and upper mantle in the India-Eurasia collision
542 zone, *Tectonics*, 35, 1642–1669, <https://doi.org/10.1002/2016TC004161>, 2016.
- 543 Turner, S., Arnaud, N., Liu, J., Rogers, N., Hawkesworth, C., Harris, N., ... and Deng, W.:



- 544 Post-collision, shoshonitic volcanism on the Tibetan Plateau: implications for convective thinning
545 of the lithosphere and the source of ocean island basalts, *Journal of petrology*, 37, 45-71,
546 <https://doi.org/10.1093/petrology/37.1.45>, 1996.
- 547 Vink G E, Morgan W J, Zhao W L: Preferential rifting of continents: a source of displaced terranes[J].
548 *Journal of Geophysical Research: Solid Earth*, 89(B12): 10072-10076,
549 <https://doi.org/10.1029/JB089iB12p10072>, 1984.
- 550 Vogt, K., Matenco, L., and Cloetingh, S.: Crustal mechanics control the geometry of mountain belts.
551 Insights from numerical modelling, *Earth and Planetary Science Letters*, 460, 12-21,
552 <https://doi.org/10.1016/j.epsl.2016.11.016>, 2017.
- 553 Vogt, K., Willingshofer, E., Matenco, L., Sokoutis, D., Gerya, T., and Cloetingh, S.: The role of lateral
554 strength contrasts in orogenesis: A 2D numerical study, *Tectonophysics*, 746, 549-561,
555 <https://doi.org/10.1016/j.tecto.2017.08.010>, 2018.
- 556 Wang, C. Y., Yang, Z. E., Luo, H., and Mooney, W. D.: Crustal structure of the northern margin of the
557 eastern Tien Shan, China, and its tectonic implications for the 1906 M~7.7 Manas earthquake,
558 *Earth and Planetary Science Letters*, 223, 187-202, <https://doi.org/10.1016/j.epsl.2004.04.015>,
559 2004.
- 560 Wang, M., and Shen, Z. K.: Present-day crustal deformation of continental China derived from GPS
561 and its tectonic implications, *Journal of Geophysical Research: Solid Earth*, 125, e2019JB018774,
562 <https://doi.org/10.1029/2019JB018774>, 2020.
- 563 Wu, Y., Bao, X., Zhang, B., Xu, Y., and Yang, W.: Seismic evidence for stepwise lithospheric
564 delamination beneath the Tibetan Plateau, *Geophysical Research Letters*, 49, e2022GL098528,
565 <https://doi.org/10.1029/2022GL098528>, 2022.
- 566 Xie, R., Chen, L., Xiong, X., Wang, K., and Yan, Z.: The Role of Pre-existing Crustal Weaknesses in
567 the Uplift of the Eastern Tibetan Plateau: 2D Thermo-Mechanical Modeling, *Tectonics*, 40,
568 e2020TC006444, <https://doi.org/10.1029/2020TC006444>, 2021.
- 569 Xie, R., Chen, L., Yin, A., Xiong, X., Chen, Y. J., Guo, Z., and Wang, K.: Two phases of crustal
570 shortening in northeastern Tibet as a result of a stronger Qaidam lithosphere during the Cenozoic
571 India–Asia collision, *Tectonics*, 42, e2022TC007261, <https://doi.org/10.1029/2022TC007261>,
572 2023.
- 573 Xu, Y., Liu, F., Liu, J., and Chen, H.: Crust and upper mantle structure beneath western China from P



574 wave travel time tomography, *Journal of Geophysical Research: Solid Earth*, 107, ESE-4,
575 <https://doi.org/10.1029/2001JB000402>, 2002.

576 Yin, A., Nie, S., Craig, P., Harrison, T. M., Ryerson, F. J., Xianglin, Q., and Geng, Y.: Late Cenozoic
577 tectonic evolution of the southern Chinese Tian Shan, *Tectonics*, 17, 1-27,
578 <https://doi.org/10.1029/97TC03140>, 1998.

579 Yin, A., and Harrison, T. M.: Geologic evolution of the Himalayan-Tibetan orogen, *Annual review of*
580 *earth and planetary sciences*, 28, 211-280, <https://doi.org/10.1146/annurev.earth.28.1.211>, 2000.

581 Zhang, Z., Deng, Y., Teng, J., Wang, C., Gao, R., Chen, Y., and Fan, W.: An overview of the crustal
582 structure of the Tibetan plateau after 35 years of deep seismic soundings, *Journal of Asian Earth*
583 *Sciences*, 40, 977-989, <https://doi.org/10.1016/j.jseaes.2010.03.010>, 2011.

584 Zhang, Z., Deng, Y., Chen, L., Wu, J., Teng, J., and Panza, G.: Seismic structure and rheology of the
585 crust under mainland China, *Gondwana Research*, 23, 1455-1483,
586 <https://doi.org/10.1016/j.gr.2012.07.010>, 2013.

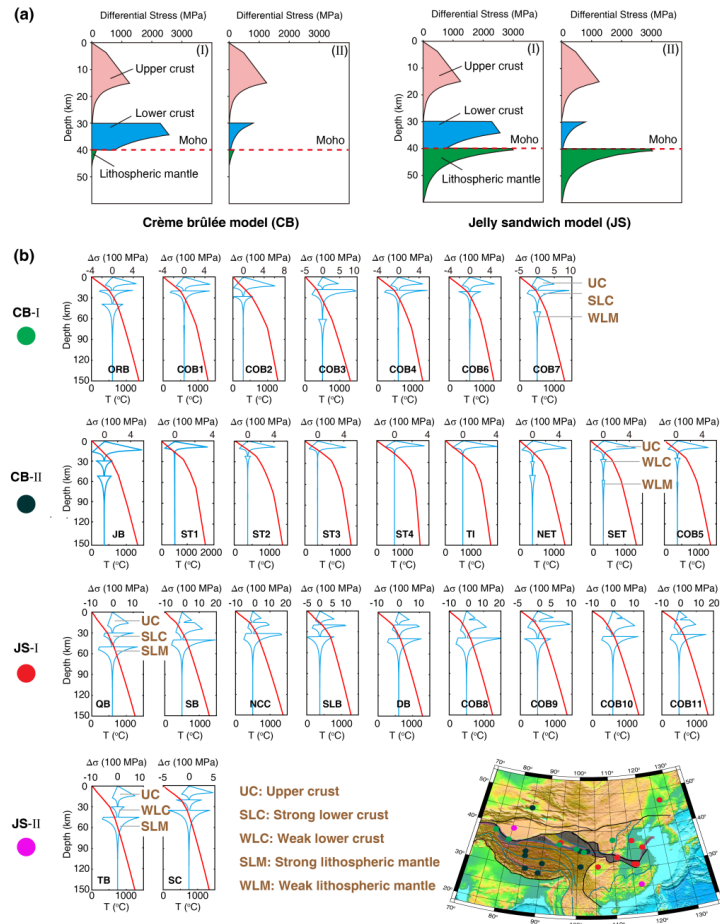
587 Zhang, Z., Teng, J., Romanelli, F., Braitenberg, C., Ding, Z., Zhang, X., ... & Panza, G. F.: Geophysical
588 constraints on the link between cratonization and orogeny: Evidence from the Tibetan Plateau and
589 the North China Craton. *Earth-Science Reviews*, 130, 1-48,
590 <https://doi.org/10.1016/j.earscirev.2013.12.005>, 2014.

591 Zhao W L, Morgan W J.: Uplift of Tibetan plateau, *Tectonics*, 4(4),
592 359-369, <https://doi.org/10.1029/TC004i004p00359>, 1985.

593
594



595 **Figures and captions**



596

597 **Figure 1. Four rheological models of continental lithosphere.** (a) Crème brûlée model (CB) and Jelly sandwich

598 model (JS). The two rheological models can be further subdivided into CB-I, CB-II, JS-I, and JS-II according to

599 the strength of the lower crust (modified from Jackson, 2002). (b) Observations of four distinct lithosphere

600 rheological structures implied for East Asia (modified from Zhang et al., 2013). Here temperature and upper and

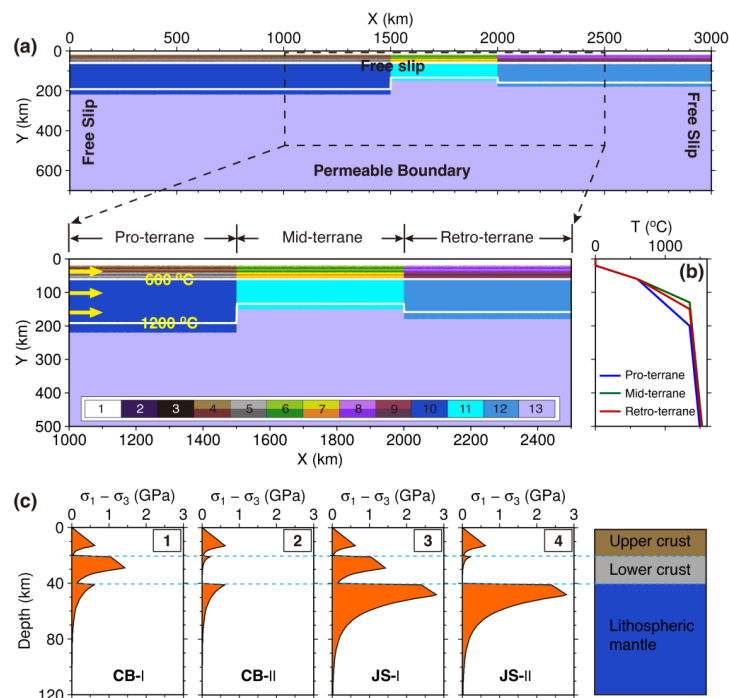
601 lower crustal composition lead to a diverse suite of strength profiles vs. depth. ORB: Ordos Basin; COB: Central

602 Orogenic Belt; JB: Junggar Basin; ST: South Tibet; TI: Tibet-INDEPTH III; NET: Northeastern Tibet; SET:

603 Southeastern Tibet; QB: Qaidam Basin; SB: Sichuan Basin; NCC: North China Craton; SLB: Songliao Basin; DB:

604 Qinling-Dabie Orogen; TB: Tarim Basin; SC: South China.

605



606

607 **Figure 2. Initial model setup.** (a) Initial model configuration. The model size is 3000 km × 700 km, and size of

608 study region is 1500 km × 500 km. Three continental terranes of the Pro-, Mid- and Retro-terrane are contained

609 in the numerical model, and they are 200 km, 130 km, and 160 km thick, respectively. White lines are isotherms

610 with an interval of 600°C. Yellow arrows indicate the convergence rate of 20 mm/yr. Colored grids: 1 – sticky air;

611 2 – sediments; 3 – weak zone; 4, 6, 8 – the upper crust of the Pro-, Mid- and Retro-terrane, respectively; 5, 7, 9 –

612 the lower crust of the Pro-, Mid- and Retro-terrane, respectively; 10, 11, 12 –lithospheric mantle of the Pro-,

613 Mid- and Retro-terrane, respectively; 13 – asthenosphere. (b) Initial temperature structure for the three terranes.

614 The Pro- and Mid-terrane respectively have a coldest and warmest lithospheric mantle due to their differences of

615 lithosphere thicknesses. (c) Four rheological models with contrasting lithospheric strength profiles. These are

616 derived from different strength scaling factor (*S*) combinations for the upper crust, lower crust, and lithospheric

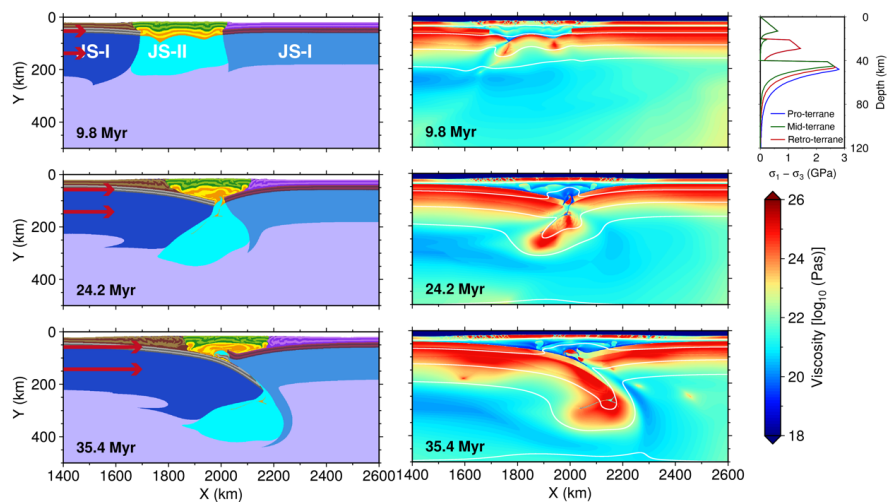
617 mantle (Table S1). Strength profiles are calculated based on the Pro-terrane's initial lithospheric structure,

618 composition, and temperature field. The prescribed strain rate is $1 \times 10^{-14} \text{ s}^{-1}$. CB-I and CB-II, the crème brûlée

619 model with strong and weak lower crust, respectively; JS-I and JS-II, the jelly sandwich model with strong and

620 weak lower crust, respectively.

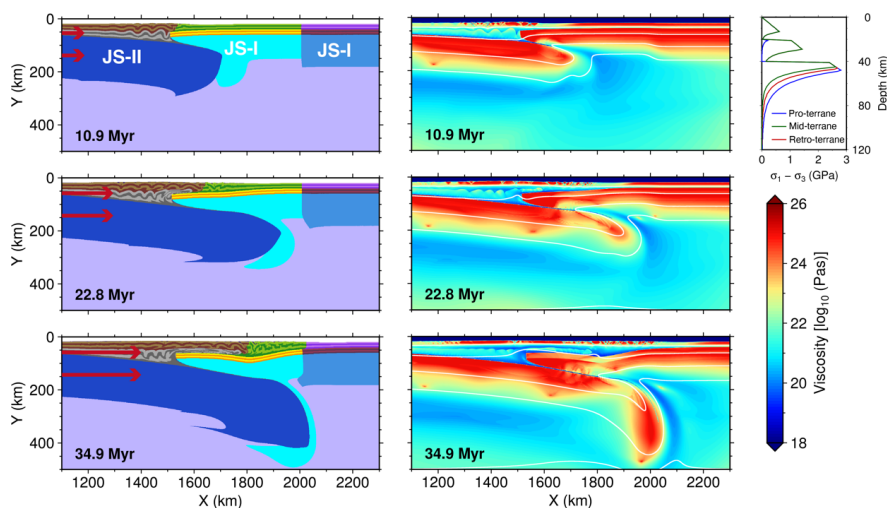
621



622

623 **Figure 3. Collision of the lithospheres of the Pro- and Retro-terrane.** Rheological models for the Pro-, Mid-
 624 and Retro-terrane are JS-I, JS-II, and JS-I, respectively, as shown in the upper right corner. The left panel shows
 625 compositional fields at 9.8 Myr, 24.2 Myr, and 35.4 Myr, respectively. The right panel shows the corresponding
 626 viscosities. White lines are isotherms with an interval of 300° C.

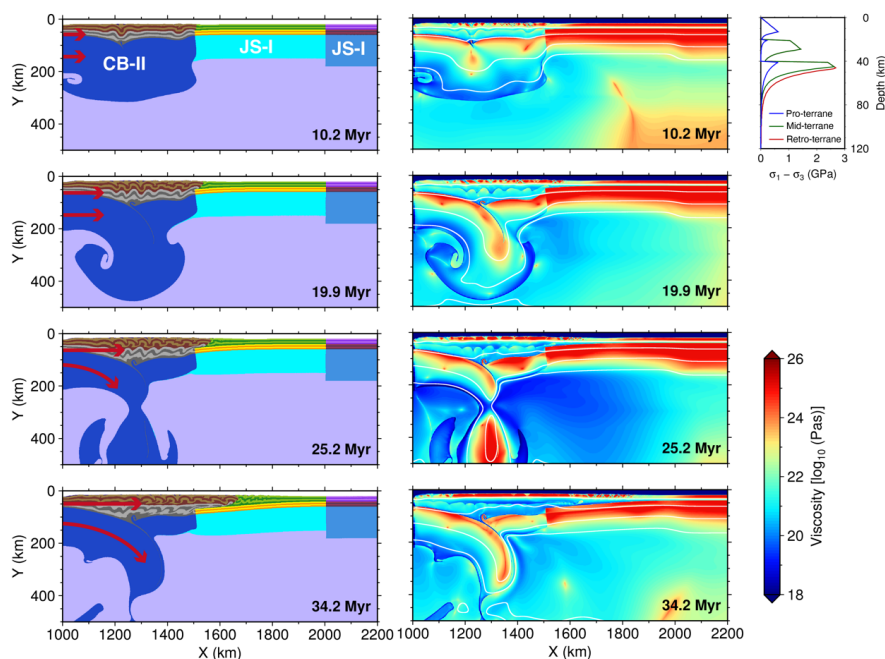
627



628

629 **Figure 4. Subduction of the lithosphere of the Pro-terrane.** Rheological models for the Pro-, Mid- and
 630 Retro-terrane are JS-II, JS-I, and JS-I, respectively. See Figure 3 for plotting conventions.

631

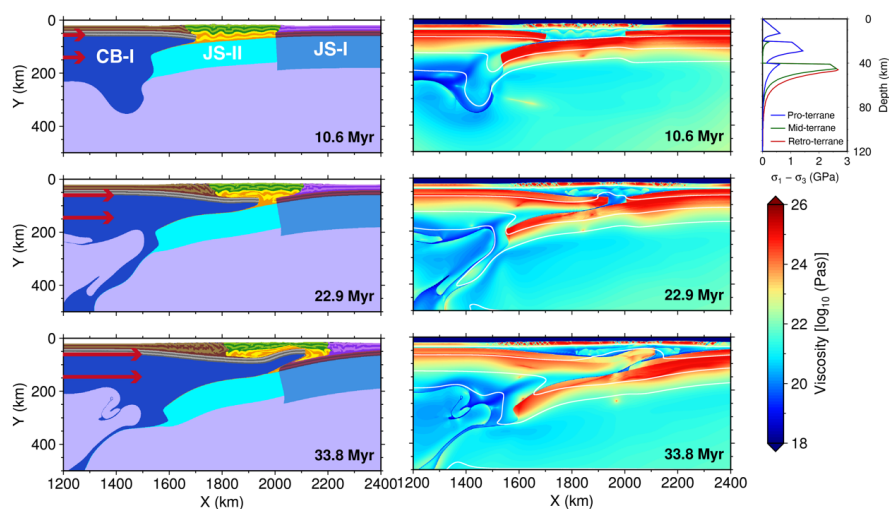


632

633 **Figure 5. Thickening and delamination of the lithosphere of the Pro-terranes.** Rheological models for the Pro-,

634 Mid- and Retro-terranes are CB-II, JS-I, and JS-I, respectively. See Figure 3 for plotting conventions.

635



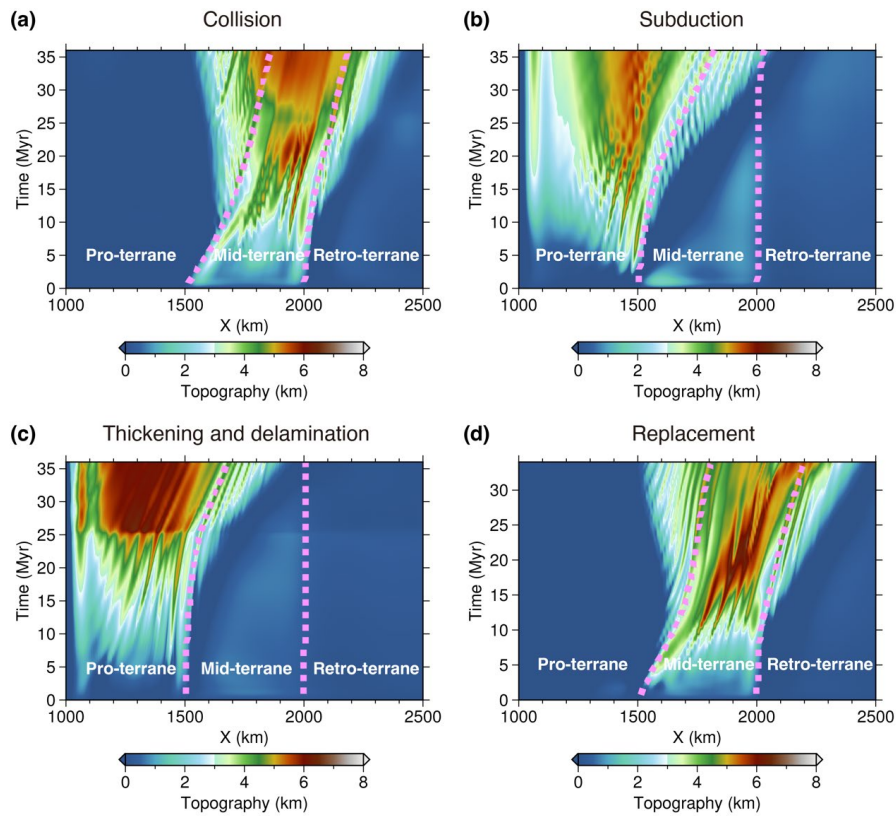
636

637 **Figure 6. Replacement of lithosphere of the Pro-terranes.** Rheological models for the Pro-, Mid- and

638 Retro-terranes are CB-I, JS-II, and JS-I, respectively. See Figure 3 for plotting conventions.



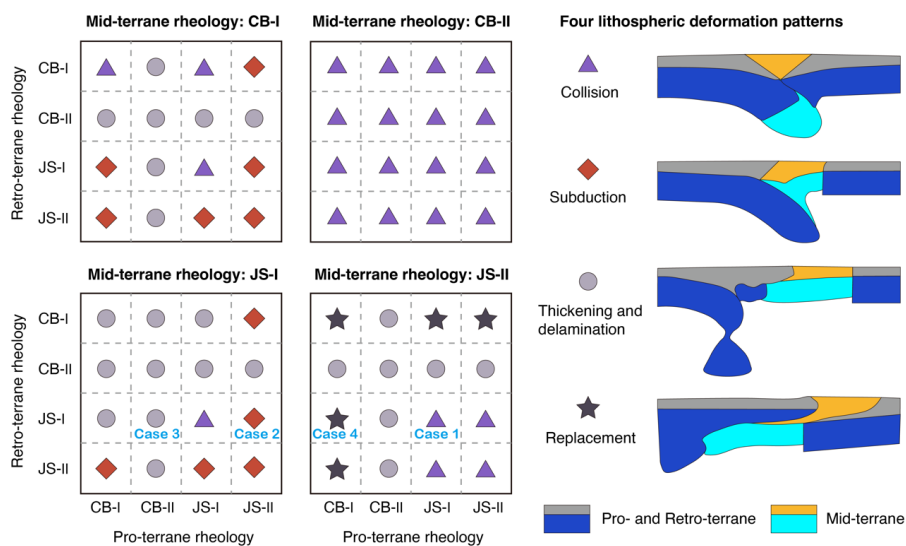
639



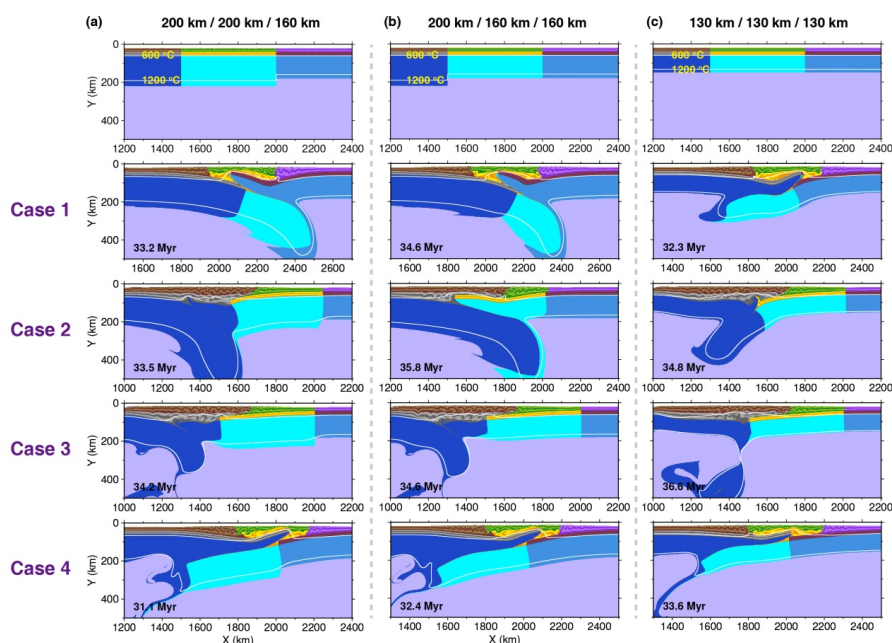
640

641 **Figure 7. Evolution of surface relief for the different deformation styles.** The purple dashed lines indicate the
642 boundaries between terranes. (a) – (d) Surface relief associated with the deformation patterns of lithosphere
643 collision, subduction, thickening and delamination, and replacement, respectively.

644



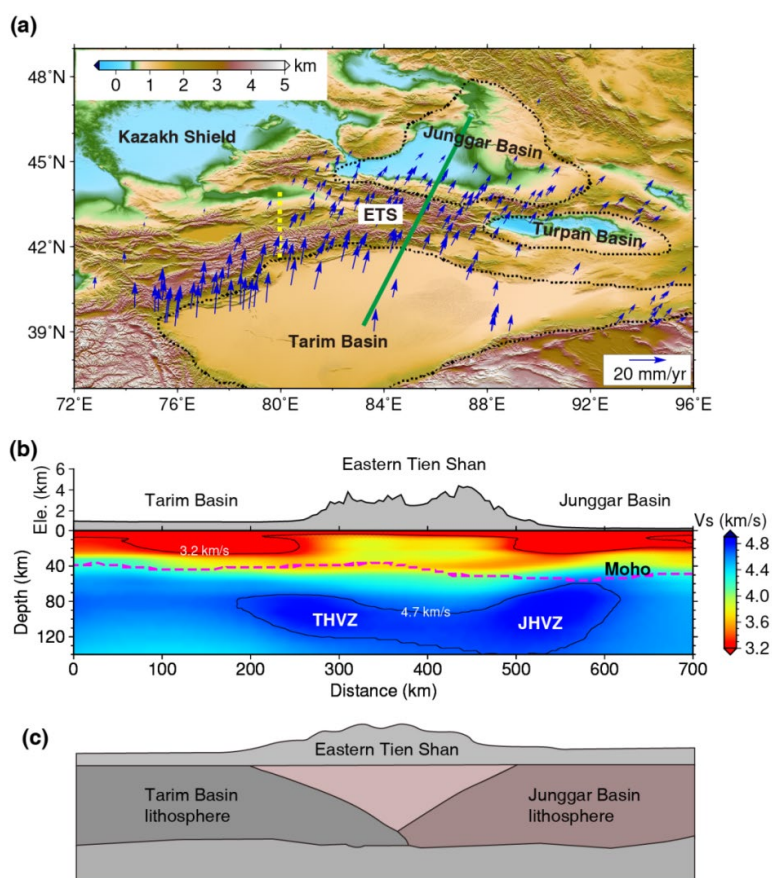
645
 646 **Figure 8. Four styles of lithosphere deformation patterns.** Symbols with colors indicate different deformation
 647 patterns of the lithosphere. Cases 1 – 4 are the selected models chosen to illustrate details of these modes of
 648 compressional evolution.
 649



650
 651 **Figure 9. Effects of lithosphere thickness variations between various terranes.** (a) – (c) Final simulation results



652 of models with the same lithosphere thicknesses of the Pro- and Mid-terranes, the Mid- and Retro-terranes, and
653 the Pro-, Mid- and Retro-terranes, respectively. Rheological models of the Pro-, Mid- and Retro-terranes in 2 – 4
654 rows are same with those in Cases 1 – 4, respectively.
655



656
657 **Figure 10. Lithosphere structure of the eastern Tien Shan.** (a) Topography and crustal movement of the eastern
658 Tien Shan and its surrounding areas. Arrows indicate GPS velocities (Wang and Shen, 2020). The yellow dashed
659 line shows the boundary of geographic longitude of 80° E. (b), (c) Vs velocities and lithosphere structure across the
660 Tarim Basin, eastern Tien Shan, and the Junggar Basin (modified from Lü et al., 2019). ETS, eastern Tien Shan;
661 THVZ, Tarim Basin high-velocity zone; JHVZ, Junggar Basin high-velocity zone.
662



663 **Table 1. Flow laws and material properties for different lithospheric layers.** ρ_0 is the initial density; it evolves
 664 with time as $\rho = \rho_0 (1 - \alpha(T - T_0))(1 + \beta(P - P_0))$, where $T_0 = 20^\circ \text{C}$, $P_0 = 10^5 \text{MPa}$. Flow law: qtz. = quartzite, Plag.
 665 = plagioclase, ol. = olivine.

Material properties	Sediment	Upper crust	Lower crust	Lithospheric mantle	Asthenosphere
ρ_0 (kg/m ³)	2600	2700	2800	3300	3300
Flow laws	Wet qtz.	Wet qtz.	Plag.	Dry ol.	Dry ol.
$1/A_D$ (Pa ⁿ s)	1.97×10^{17}	1.97×10^{17}	4.80×10^{22}	3.98×10^{16}	3.98×10^{16}
n	2.3	2.3	3.2	3.5	3.5
E_a (KJ/mol)	154	154	238	532	532
V_a (J/bar)	0.8	0.8	1.2	1.2	1.2
$\phi = \sin(\varphi)$	0.2 – 0.1	0.3 – 0.1	0.3 – 0.1	0.6 – 0.4	0.6 – 0.3
C (Pa)	$1 \times 10^{7-6}$	$1 \times 10^{7-6}$	$1 \times 10^{7-6}$	$1 \times 10^{7-6}$	$1 \times 10^{7-6}$
H_r (uW/m ³)	2.0	1.5	0.5	0.022	0.022
C_p (J/kg K)	1000	1000	1000	1000	1000
α (1/K)	3×10^{-5}	3×10^{-5}	3×10^{-5}	3×10^{-5}	3×10^{-5}
β (1/MPa)	1×10^{-5}	1×10^{-5}	1×10^{-5}	1×10^{-5}	1×10^{-5}
k (W/m/K)	$0.64 + 807/(T+77)$	$0.64 + 807/(T+77)$	$1.18 + 474/(T+77)$	$[0.73 + 1293/(T+77)] \times (1 + 0.00004P)$	$[0.73 + 1293/(T+77)] \times (1 + 0.00004)$

666